BACHELOR THESIS

EXPERIMENTAL VALIDATION OF THE BOUNDEDNESS OF HELICAL MICROROBOTS

Louisa Madeleine Hafferl

DEPARTMENT OF BIOMECHANICAL ENGINEERING
ISLAM KHALIL

EXAMINATION COMMITTEE
Constantinos Goulas
Arvid Keemink

DOCUMENT NUMBER
BE - 960

UNIVERSITY OF TWENTE.

24/09/23

Abstract

In this thesis, the input-output stability problem of controlling magnetically driven helical microrobots is analyzed to achieve bounded straight runs without drift in a low-Reynolds-number regime. An active suspension solution is found experimentally, yielding helical propulsion with a near-zero angle of attack without drift, though the theoretical modelling remains inconclusive. Unique control inputs are found, for a given helical microrobot geometry and material composition, which can be generated with rotating field.

Contents

1 Introduction **2**
1.1 Problem Formulation . . . 2
1.2 Research Question and Approach . . . 2

2 Theory **4**
2.1 Boundedness . . . 4
2.2 Gain . . . 4

3 Characterization **5**
3.1 Geometry - SEM Imaging . . . 5
3.2 Material Properties . . . 6
3.2.1 Energy Dispersive X-Ray Spectroscopy (EDX) . . . 6
3.2.2 Inconsistencies . . . 7
3.3 Theoretical Composition . . . 7
3.3.1 Volume Calculation . . . 7
3.3.2 Weight Percentages . . . 9
3.4 Magnetic Properties . . . 10
3.4.1 Magnetic Dipole Moment . . . 10
3.4.2 Magnetic Behaviour of Components . . . 10
3.4.3 Magnetic Dipole Moment Calculation . . . 11

4 Modelling **12**
4.1 MATLAB . . . 12
4.1.1 Procedure and Results . . . 12
4.2 COMSOL . . . 13
4.2.1 Description . . . 13
4.2.2 Results . . . 14

5 Experimental Method **15**
5.1 Description . . . 15
5.2 Setup and Design . . . 15
5.2.1 Cuvettes/Containment . . . 15
5.2.2 Keyence Microscope . . . 16
5.2.3 Rotating Permanent Magnet . . . 16
5.2.4 Additional Equipment . . . 17
5.2.5 Setup Overview and Limitations . . . 17
5.3 Experimental Procedure . . . 18
5.3.1 Noted Interferences . . . 18
5.3.2 Measurement Method . . . 18
5.4 Processing . . . 18
5.5 Results . . . 19

6 Conclusion **21**
6.1 Conclusion . . . 21
6.2 Further Work . . . 21

Chapter 1

Introduction

1.1 Problem Formulation

The term microrobots this thesis refers specifically to Untethered Helical Magnetic Devices (UHMDs), helical robots that are actuated wirelessly via a rotating magnetic field to induce rotational movement [1].These UHMDs have many possible biomedical applications, including tissue penetration, drug delivery and targeted therapy [2]. The usage on which this research is centered is the application of micro UHMDs to dissolve blood clots.

Blood clots (thrombus) are a method with which the body prevents excessive bleeding when a blood vessel is injured. Usually, these clots are dissolved naturally when the wound heals, but cases where clots form inside of blood vessels without dissolving naturally are possible. These clots can happen in deep veins of the body, or break free and move around the arteries (becoming an embolus), leading to dangerous medical conditions, such as Venous Thromboembolism (VTE) [3].

The use of UHMDs for grinding and dissolving these blood clots has been widely explored, although the methods to control said UHMD vary. One of the primary challenges in their application is the loss of feedback when the UHMDs are introduced in vivo. Visual feedback is lost, and although using ultrasound is possible and has been demonstrated in vitro [4], simplifying the process can make it more attainable.

In order to mitigate the effect of the loss of feedback during in vivo applications, the behaviour of the UHMD must be either perfectly predictable (with behaviour fully and accurately modelled), or guaranteed (bounded by rotational magnetic actuation). The boundedness of helical microrobots has been studied in order to achieve motion control systems of microrobots based on their location, without orientation localisation.

The use of helical microrobots with a diameter of $300\mu m$ has been validated with in vitrio experiments to clear clogged blood vessels [5], using two rotating dipole fields as mechanical actuation, instead of the one rotating magnet arm intended for this research.

Using a robotic arm, to which a permanent magnet is attached, the rotation of the magnetic field can be controlled in a way to bound the UHMD, allowing it to propel itself through viscous fluids. Input-output boundedness of the states of the helical device have been demonstrated for mm size, meaning that there is a potential to enable predictable motion, even with sensory uncertainties during localization [2]. However, to further the application of the control of the UHMDs with a singular rotating magnet to the human body, an attempt is to be made to control robots at a micro-size and determine if they can reach bounded behaviour.

1.2 Research Question and Approach

The purpose of this research is to attempt to apply established motion control of millimeter-sized UHMDs to micro-sized UHMDs and examine differences between the modelled and measured propulsion of the microrobot.

The research question proposed for this thesis is the following: Is it possible to validate the boundedness of helical microrobots predicted with a previously designed model for millimeter-sized helical microrobots?

This research question is then broken down into the following questions: Can the previously designed model predict bounded behaviour from the microrobots? Can bounded responses be obtained experimentally with the helical microrobots? Does the model accurately predict the witnessed behaviour?

This will be answered by determining the characteristics with which to model the microrobots behaviour, and studying their theoretical behaviour. Then, these microrobots will be placed in tubes and actuated using a robotic arm with a permanent magnet (creating rotating magnetic fields) in an attempt to control the motion of the helical microrobot, experimentally.

This research will be described in this report, following the process of the necessary activities: A look into the theoretical aspects of the research as well as the theoretical model, experimental research, and an analysis of the observed behavior.

Chapter 2

Theory

2.1 Boundedness

A UHMD placed into a fluid will simply float downwards, but by introducing a Rotating Permanent Magnet (RPM) to actuate it, an external magnetic torque can be applied, compensating for the force of gravity and allowing the UHMD to move horizontally.

Placing the RPM at a point $\mathbf{p}_{\mathrm{a}}$ with respect to the frame of reference, rotating around its axis $\boldsymbol{\Omega}_{\mathrm{a}}$ at a frequency $\mathrm{f_a}$, with a pitch angle of β_a with respect to the x-axis, causes the UHMD, located at point $\mathbf{p}_{\mathrm{h}}$ from the frame of reference, to rotate at a frequency $\mathrm{f_h}$ around its axis $\boldsymbol{\omega}_h$. The angle β_h formed between $\boldsymbol{\omega}_h$ and the x-axis is also referred to as the angle of attack [6] [2].

The effect of this time-dependent torque and force on the UHMD generates a propulsion, (with a velocity $\mathbf{v}_a$) characterized by the position of the UHMD from the RPM:

${}^{\mathrm{a}}\mathbf{p}_{\mathrm{h}} = [{}^{\mathrm{a}}\mathbf{p}_{\mathrm{h_x}}, {}^{\mathrm{a}}\mathbf{p}_{\mathrm{h_y}}, {}^{\mathrm{a}}\mathbf{p}_{\mathrm{h_z}}]$

In the limit of low-Reynolds number (which is to say, a system with smooth, constant fluid motion), the force balance between external non-fluidic and viscous forces and torques can predict the rotation rate of the UHMD and its velocity [2] [6]:

$$\left(\begin{bmatrix} (\mathbf{m}_h \cdot \nabla)\mathbf{B}({}^{\mathrm{a}}\mathbf{p}_{\mathrm{h}}) + \mathbf{f}_{visc} + \mathbf{f}_g \\ \mathbf{m}_h \times \mathbf{B}({}^{\mathrm{a}}\mathbf{p}_{\mathrm{h}}) + \boldsymbol{\tau}_{visc} + \boldsymbol{\tau}_g \end{bmatrix}\right) = 0 \qquad (2.1)$$

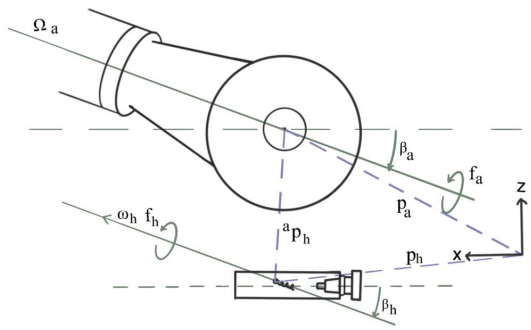

Figure 2.1: Diagram representing the positions and vectors used to define the movement of a UHMD.

where $\mathbf{f}_{visc}$ is the drag force and $\mathbf{f}_g$ is the gravitational force, and $\boldsymbol{\tau}_{visc}$ and $\boldsymbol{\tau}_g$ are their corresponding torques. $\mathbf{m}_h$ is the magnetic dipole moment of the helix (further explained in Section 3.4), with $\mathbf{B}({}^{\mathrm{a}}\mathbf{p}_{\mathrm{h}})$ representing the strength of the magnetic field, $\mathbf{B}$, at the position of the UHMD, ${}^{\mathrm{a}}\mathbf{p}_{\mathrm{h}}$. With this force balance, the translational velocity v_h and angular velocity of the UHMD can be determined for a given $\mathbf{m}_h$ and ${}^{\mathrm{a}}\mathbf{p}_{\mathrm{h}}$.

2.2 Gain

Boundedness, or a bounded response, is defined when the trajectory of the UHMD remains constant for all future time, with a perfect force balance and no drift. In order to quantify this, a gain is defined: the ratio between the initial total change in the trajectory of the UHMD to its initial distance to the RPM [2] [6]:

$$\gamma := \frac{\min({}^{\mathrm{a}}p_{\mathrm{h}_z}(t)) - \max({}^{\mathrm{a}}p_{\mathrm{h}_z}(t))}{{}^{\mathrm{a}}p_{\mathrm{h}_z}(t_0)} \qquad (2.2)$$

Chapter 3

Characterization

The microrobots used throughout this thesis were 3D micro-printed onto a substrate using Direct Laser Writing with an IP-Dip photoresin and then sputtered with a layer of approx $300nm$ of Nickel, followed by $50nm$ of Gold as an inert protective layer to prevent corrosion. They are shaped to have a spherical head attached to a helical tail.

In order to predict the behaviour of these microrobots when actuated by a uniform magnetic field (a rotating permanent magnet) to swim in a low-density liquid, the microrobots geometric dimensions and magnetic properties are necessary. Specifically the dimensions from which the volume and drag can be computed (diameter of the head, diameter of the wire, diameter of the coil loop, the length of the microrobot and the spacing between the helix loops), and the magnetic properties that can describe it's interaction with the magnetic field (the dipole moment).

3.1 Geometry - SEM Imaging

The geometric dimensions of the UHMDs were determined visually from a microscopic image of a collection of microrobots made by Scanning Electron Microscopy, which uses a focused beam of electrons instead of light to scan a surface and form an image. This beam is produced by an electron gun and travels vertically down a vacuum in the microscope, passing through lenses and electromagnetic fields that focus it to the sample placed in the microscope. The beam interacts with the surface of the sample, causing electrons and X-rays to be ejected from the sample. These are collected by detectors inside the microscope and produce a signal containing information about the surface topography of the sample. The position of the beam and the intensity of this signal are sent to a screen to produce an image of the sample [7] [8]. For SEM to be successful, the samples used must be electrically conductive and electrically grounded to avoid the accumulation of electric charge from the beam, as this effect leads to image distortion [9].

SEM imaging was chosen over the use of a normal optical microscope as it has a higher resolution and magnification and the UHMDs fulfilled the conductivity condition (having been sputtered in conductive metals), making it the better choice for determining the dimensions of the microrobot [10]. Three different SEM measurements were taken by Constantinos Goulas and Islam Khalil with the NeoScope JCM-5000 bench top Scanning Electron Microscope at the MS3 department of the University of Twente, at three different magnifications: 275x, 420x and 1350x as shown in Figures 3.1a, 3.1b and 3.1c respectively.

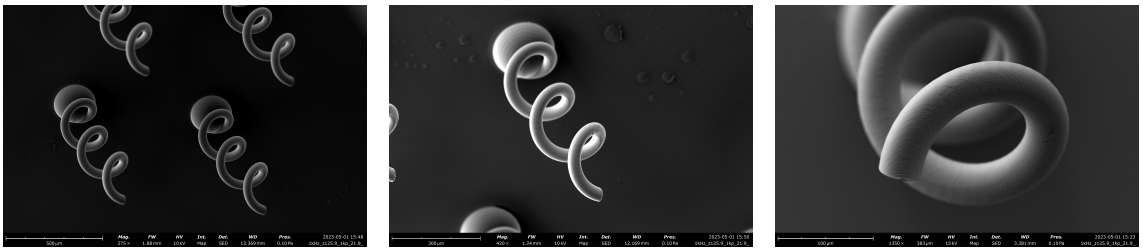

(a) (b) (c)

Figure 3.1: Results of the SEM, showing (a) various microrobots on a plate background, (b) a magnified image of one microrobot, (c) a magnified image focused on the tail end of a microrobot

The parameters necessary to describe the geometry of the microrobots were then determined

SEM		EDX	
L [μ m]	500 ±50	Ni [Wt%]	61.8 ±0.6
d_s [μm]	200 ±10	Au [Wt%]	23.7 ±1.2
d_w [μm]	45 ±3	C [Wt%]	11.25 ±1.3
p [μm]	180 ±20	O [Wt%]	3.2 ±0.4
d_h [μm]	200 ±6		

Table 3.1: Geometric and Material Properties as characterized by Scanning Electron Microscopy (SEM) and Energy-Dispersive X-Ray Spectroscopy (EDX)

by processing these images in the video tracking software *Tracker*. The scale bar included in the SEM results was used to calibrate the distance tracking function of the software, and then xx parameters were determined: the length if the helical coil (L), the diameter of the spherical head (d_s), the diameter of the wire used in the coil (d_w), the distance between the loops of the coil (pitch, p) and the diameter of the loops of the helix (d_h), as shown in Figure 3.1.

The distances were measured multiple times, in the different images and from different points in the image, in order to get a more accurate value. However, as the angle at which the SEM images were taken was unknown, the distortion of the measured distances caused by said angle was not taken into account. This is represented most clearly by the larger standard deviation in the determined values of L and p, where this angle has the largest effect, leading to a larger variation in the measurements in different images.

3.2 Material Properties

The most straightforward method to determine the magnetic properties (namely the magnetic dipole moment) of a sample such as the UHMD would be via Vibrating Sample Magnetometry (VSM).

VSM is a technique used to determine the magnetic moment of a sample when vibrated in a uniform magnetizing field, based on Faraday's law of magnetic induction. The sample is placed between electromagnet poles oriented perpendicularly to the magnetizing field, and a constant vibration is applied. The moment of the sample creates a magnetic field that changes as a function of time. This magnetic flux, proportional to the magnetic moment of the sample, varies, leading to an induce AC voltage in pickup coils placed near the poles. This induced voltage is measured to obtain information about the magnetic moment of the sample. The result of a VSM measurement is a magnetization curve, from which the magnetic properties can be deduced.

However, apart from the fact that VSM measurements require sample sizes larger than the available microrobots, the main disadvantage of this process is that it is not suitable for fragile samples due to the acceleration occurring during vibration. As there were only three (very fragile) microrobots available for the measurement and experimentation process, VSM measurements were deemed unfeasible. Instead, the magnetic dipole moment of the microrobots was to be determined theoretically from the material composition of the UHMD. This material composition was initially determined via Energy Dispersive X-Ray Spectroscopy (EDX) [11], then checked by a calculation of the theoretical volumes of materials according to the description of the UHMD fabrication.

3.2.1 Energy Dispersive X-Ray Spectroscopy (EDX)

Energy Dispersive X-Ray Spectroscopy (EDX) is a method used to quantify the elemental composition of a sample of material. EDX detects the X-rays produced during SEM imaging, when an electron beam interacts with the surface of an input sample (as explained in Section 3.1). These X-rays have a wavelength that is characteristic of the atomic structure of the elements of the sample. The results of EDX are shown as a spectrum, displaying peaks of energy levels for which most X-rays have been received. Each peak corresponds to an atom, and therefore an element, so the height of the peak indicated the concentration of the element in the sample, as shown in Figure 3.2 [12] [13].

EDX measurements were carried out with the same sample plate as in the SEM measurements, containing multiple microrobots. However, during the time between these procedures, the container with the microrobots had been handled roughly, and the fragile microrobots inside of it (which had been standing upright) snapped. Therefore, the EDX measurements were focused on one of the remaining intact heads of a microrobot, with the longest remaining piece of helix still attached. The results of the EDX measurements taken by Nick Helthuis at the MS3 Microscopy Lab at the

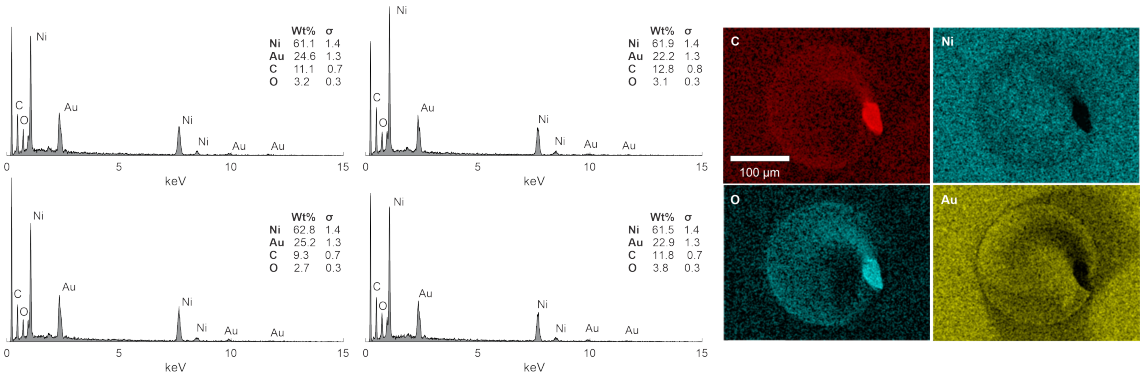

Figure 3.2: EDX Results

University of Twente are shown in Figure 3.2. Four measurements on different points of the sample resulted in four different spectrum graphs with varying weight percentages, of which the average and standard deviation were taken for Figure 3.1. Included in Figure 3.2 are also four differently colored images of the sample, showing the concentration of specific elements per pixel of the image.

3.2.2 Inconsistencies

As in SEM, during EDX the interaction between the electron beam and the sample occur in a teardrop-shaped volume extending below the surface. In most measurements this means this depth leads to a more accurate reading of the composition in EDX, but for a maximum sample of a depth of $200\mu m$ (the radius of the head) this interaction volume could have included part of the plate on which the microrobots were placed. As the size of the interaction volume during the measurements was unknown, the extent of this effect is unknown.

Furthermore, as is visible in the images in Figure 3.2, the center of the broken-off piece, made entirely of IP-DIP photoresist has a higher thickness than the layers of Ni and Au surrounding it, which correlates with the fact that the metal layers were sputtered on to a much wider photoresist component. This implies that the $Wt\%$ of C and O should be larger than what is indicated by the measured values, as they represent a larger part of the composition.

For these reasons, an analysis of the material composition as described by the fabrication process was carried out (Section 3.3), to determine if the EDX results could be supported theoretically (by the description of the fabrication of the microrobt) or if more inconsistencies became apparent.

3.3 Theoretical Composition

In order to assess to what extent the weight percentages determined by the EDX had been influenced by the gold plate holding the sample and the incompleteness of the robot, the description of the fabrication of the microrobots was used to estimate what the weight percentages of the elements would be from the layers sputtered onto the substrate.

The microrobots were 3D micro-printed with Nanoscribe out of an IP-Dip photoresin, and deposited with metallic layers: $300nm$ of Ni (th_{Ni}) and $50nm$ of Au (th_{Au}). The measurements of the EDX show highest percentages of Ni and Au, corresponding with the thickness of the sputtered layers, and lesser C and O percentages, (representing the organic components of the photoresin polymer).

To calculate the weight percentages of Ni, Au, and the photoresin (a combination of C&O) according to this description of the layers of the components of the microrobot, the volume of each layer was determined. This was done in a Matlab script, by calculating the volume of the spherical head and helix as described by the parameters determined in the SEM measurement, and then subtracting volumes calculated with the different thicknesses in layers. The volumes were then converted to weight percentages by considering the densities of the materials.

3.3.1 Volume Calculation

Spherical Head Volumes

To determine the volumes of the different layers of the sphere, the volumes of three different spheres (as shown in Figure 3.3) were calculated: Sphere A, with the radius as measured in the

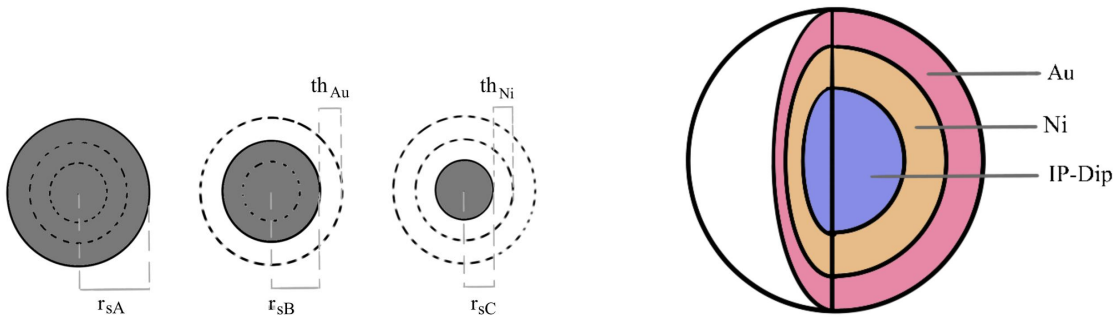

(a) (b)

Figure 3.3: Diagram (a) included to define the volumes (2D images of spheres A, B and C from left to right) and parameters used in the calculation of the volumes of the layers defined as shown in diagram (b)

SEM ($r_{sA} = d_s/2$); Sphere B, with the radius of Sphere A minus the thickness of the Nickel layer ($r_{sB} = d_s/2 - th_{Ni}$); Sphere C, with the radius of Sphere B minus the thickness of the Gold layer ($r_{sC} = d_s/2 - th_{Ni} - th_{Au}$).

$$V_{sphere} = \frac{4}{3}\pi r_s^3 \tag{3.1}$$

After determining these spherical volumes (V_{sA}, V_{sB}, V_{sC}) with the formula shown above, the volumes of each of the layers (Gold V_{Au}, Nickel V_{Ni} and Photoresin V_{CO}) were as shown below:

$$V_{sCO} = V_{sC} = \frac{4}{3}\pi(d_s/2 - th_{Ni} - th_{Au})^3 \tag{3.2}$$

$$V_{sNi} = V_{sB} - V_{sC} = \frac{4}{3}\pi(d_s/2 - th_{Ni})^3 - \frac{4}{3}\pi(d_s/2 - th_{Ni} - th_{Au})^3 \tag{3.3}$$

$$V_{sAu} = V_{sA} - V_{sB} = \frac{4}{3}\pi(d_s/2)^3 - \frac{4}{3}\pi(d_s/2 - th_{Ni})^3 \tag{3.4}$$

These layered volumes of the spherical head are then combined with the volumes of the layers in the helix.

Helix Volumes

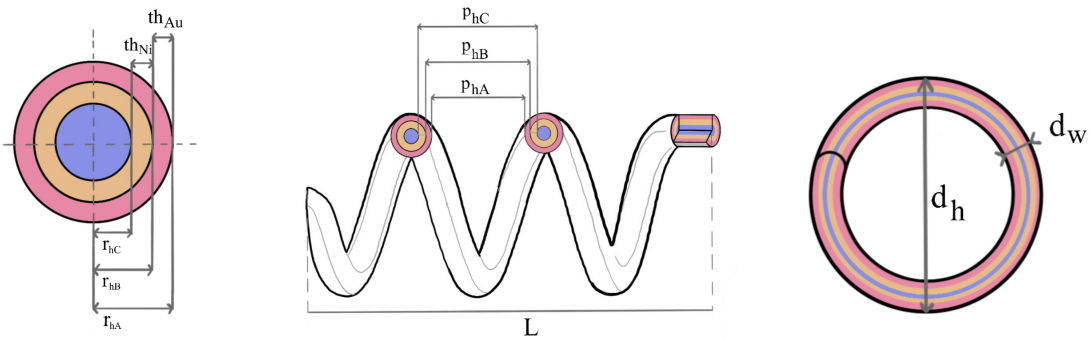

(a) (b) (c)

Figure 3.4: Diagram (a) shows a cross section of the helix wire and parameters used in the calculation of the helical volumes A, B and C. Diagram (b) shows a diagram of the length of the coil, as well as the way the pitch for volumes A, B and C are defined. Diagram (c) is a vertical view of the helix, and defines the diameter of the helix loop and that of the wire.

The same method as used for the spherical head of the microrobot is used to determine the volumes of the layers of the helix. Three volumes are defined as A, B and C with wire radii as shown in Figure 3.4 (a), where volume A is the largest, B is the one reduced by a layer, and C is the smallest volume. The formula for the volume of a helix (given below) requires the diameter of the wire (d_w) and the total length of the wire (W).

$$V_{helix} = \frac{\pi d_{wire}^2 W}{4} \tag{3.5}$$

$$W = \frac{L}{p + d_{wire}} \sqrt{\pi (d_{helix})^2 + s} \tag{3.6}$$

Where L is the measured height of the wire, s is the pitch, d_{wire} is the diameter of the wire used in the coil, and d_{helix} is the diameter of the coil as shown in figure 3.4 (c). These variables are slightly different for each of the helix volumes A (V_{hA}), B (V_{hB}) and C (V_{hC}), as summarized in Table 3.2, in terms of the measured SEM parameters (L, d_s d_w, p and d_h):

	V_{hA}	V_{hB}	V_{hC}
d_{wire}	d_w	$d_w - 2th_{Au}$	$d_w - 2(th_{Au} + th_{Ni})$
s	p	$p + 2th_{Au}$	$p + 2(th_{Au} + th_{Ni})$
d_{helix}	d_h	$d_h - 2th_{Au}$	$d_h - 2(th_Au + th_{Ni})$

Table 3.2: Table summarizing parameters used for the calculation of three different helical volumes (V_{hA}, V_{hB} and V_{hC}).

From these volumes, the volumes of the layers of Gold, Nickel and IP-Dip Photoresist were determined with the same method as the previous section, having used the parameters assigned in Table 3.2, to calculate the volumes shown in Table 3.3:

$$V_{hCO} = V_{hC} \tag{3.7}$$

$$V_{hNi} = V_{hB} - V_{sC} \tag{3.8}$$

$$V_{hAu} = V_{hA} - V_{sB} \tag{3.9}$$

3.3.2 Weight Percentages

The volume of the physical microrobot is determined from combining the spherical volume V_{sA} and the helical volume V_{hA}, as these were calculated directly from the dimensions determined via SEM. This results in a total volume of $7.1 * 10^6 \mu m^3$. With the aim of comparing these calculated volumes of the layers to the weight percentages determined by the EDX, these volumes are then converted to weight percentages.

Weight Percentage ($Wt\%$) is defined as the ratio between the mass of a substrate (m_i) and the total mass of the mixture (w_t), represented as:

$$Wt\% = \frac{m_i}{m_t} 100 \tag{3.10}$$

A conversion from the determined volumes requires the density of each of the components, a calculation for the mass associated to each volume, and a calculation of the total mass. The density of nickel and gold at room temperature (25-30 degrees) are respectively $8.90 g/cm^3$ [14] and $19.32 g/cm^3$ [15]. The density of IP-DIP Photoresist according to the Nanoscribe Material Datasheet [16] is $1.17 g/cm^3$.

The mass associated with each volume was determined with the relation between volume, density and mass: $Mass = \frac{Volume}{Density}$, and the total mass was determined as the sum of these. These results and the corresponding weight percentages are summarized in Table 3.3.

The weight percentages determined from the description of the fabrication of the microrobots shown in Table 3.3 are vastly different from those measured during the EDX. But even taking into consideration the likely wear and tear of the layers on the microrobots, and the possible

[h]	Theoretical Volume [m^3]	Theoretical [Wt%]	EDX [Wt%]
Ni	2.0×10^{-13}	18	61.8 ± 0.6
Au	1.2×10^{-14}	2	2.7 ± 1.2
C&O	6.8×10^{-12}	80	14.4 ± 1.5

Table 3.3: Summary of the theoretically determined volumes and weight percentages for the different layers of components. The carbon and oxygen readings are presented combined, as a representation of the IP-Dip photoresist.

inconsistencies that could have partially led to this divergence (mentioned in Section 3.2.2) the difference is still significant enough to be concerning. The results of the theoretical may not be experimentally supported, but conceptually align with the structure of the microrobot in a way that the EDX results do not: the $Wt\%$ of CO is larger than Nickel and Gold, reflecting that most of the microrobot was micro-printed out of a photoresin polymer, with the metals added as thin covering layers. Therefore, although the theoretical weighted percentages may not be as precise as those determined by the EDX, they are assumed to be more accurate and will be used for the succeeding sections.

3.4 Magnetic Properties

The property necessary to characterise the magnetic behaviour of the UHMD when introduced to a magnetic field is the magnetic dipole moment.

3.4.1 Magnetic Dipole Moment

The magnetic dipole moment ($\mathbf{m}$) describes the magnetic strength of an object, and can be defined as a vector relating the aligning torque ($\boldsymbol{\tau}$) on said object from an applied magnetic field ($\mathbf{B}$).

$$\boldsymbol{\tau} = \mathbf{m} \times \mathbf{B} \tag{3.11}$$

In a uniform magnetic field, such as the one to be applied to the UHMD, when the dipole direction is perpendicular to the magnetic field (θ), the maximum amount of torque on the dipole is proportional to the magnetic moment (m) [17]:

$$\boldsymbol{\tau} = m \cdot B \cdot \sin\theta \tag{3.12}$$

Materials with any amount of magnetism have atoms with permanent and temporary dipole moments, the way these moments are oriented depends on the property of the material (paramagnetic, ferromagnetic, diamagnetic, etc), unless the material is in an external magnetic field (B), where the dipoles tend to align with said field. The alignment in a volume (V) of material is measured as Magnetization (M):

$$Magnetisation = M = \frac{m}{V} \tag{3.13}$$

The maximum magnetic moment per unit volume for a magnetic material is called the Saturation Magnetisation (Amperes/meter). At this point most of the magnetic moments are aligned in the same direction as the field. The saturation magnetisation is a material property usually seen on a B-H curve (or Magnetisation curve), where the B-field in a material is measured as function of a changing H-field. By using the above equation with the saturation magnetisation, the magnetic moment of the material under a strong magnetic field can be estimated [18].

3.4.2 Magnetic Behaviour of Components

In order to determine the magnetic dipole moment of the microrobot, first the magnetic properties of its components (gold, nickel and the IP-DIP photoresin) are studied.

Diamagnetic materials only react weakly to magnetic fields, usually forming magnetic dipoles directed opposite the external field, with forces weak enough to require sensitive equipment to measure. Gold is diamagnetic at large sizes, although it can exhibit paramagnetic behaviour at nano-particle size or in nano-agglomerates [19]. However, taking into consideration that the layer of gold was added to the UHMD not for its magnetic properties but to prevent corrosion, it is unlikely that the usual diamagnetic properties noted at bulk sizes would be distinguishable or predictable.

The magnetic properties of IP-Dip photoresin are not included in its Material Datasheet, but like most polymers, it can be assumed to be non-magnetic (unaffected by magnetic fields) [20].

Nickel is a ferromagnetic material, which is to say, it is very attracted to magnets and reacts strongly in magnetic fields. In the case of the microrobots, it acts as a soft magnet: easily magnetised and easily demagnetised. It is the main magnetic component added as a layer to the microrobot for its magnetic properties [21]. The saturation magnetisation of pure Nickel at room temperature has been measured to be 55.1 emu/g [14]. This means that for the calculation of the magnetic dipole moment of the microrobot, nickel is the most significant component.

3.4.3 Magnetic Dipole Moment Calculation

To calculate the magnetic dipole moment of the volume of nickel layer on the microrobot, the magnetisation saturation $55.1emu/g$ is first converted to A/m, by multiplying it by the density of nickel ($8.90g/cm^3$). This gives a saturation magnetisation of $4.7e5A/m$.

Reordering the Equation 3.14, and using the previously calculated volume of nickel, the estimation of the magnetic dipole moment gives:

$$m = M \cdot V = 9.4 \times 10^{-8} Am^2 \tag{3.14}$$

Chapter 4

Modelling

4.1 MATLAB

The premise of this thesis was to find whether a previously designed model, specifically one used for millimeter-sized robots actuated by a singular rotating permanent magnet [2] could be applied to micro-sized robots to accurately predict their trajectories, leading to a controlled and bounded motion for the microrobot both experimentally and theoretically.

The model used in this thesis was designed by Leendert-Jan W. Ligtenberg and used in his paper "Input-Output Boundedness of a Magnetically-Actuated Helical Device".

It applies the force balance defined in Section 2.1, to a situation in which a UHMD follows a rotating RPM drawing a circular trajectory, further defining the pose of the RPM with:

$$\mathbf{p}_a(t) = \mathbf{R}_a(\beta_a, \dot{\gamma}_a, t)\mathbf{p}_a(t_0) + \mathbf{v}_a t \tag{4.1}$$

$$\boldsymbol{\Omega_a(t)} = \mathbf{R}_a(\beta_a, \dot{\gamma}_a, t)\boldsymbol{\Omega_a(t_0)} \tag{4.2}$$

Where $\mathbf{p}_a(t)$ is the position of the RPM and $\boldsymbol{\Omega}_a(t)$ is the rotation axis of the RPM, at a point in time t. t_0 specifies the initial time, and v_a the velocity of the RPM. $\mathbf{R}_a(\beta_a, \dot{\gamma}_a, t)$ represents a rotation matrix specified below, in terms of the pitch angle β_a, the change in yaw angle $\dot{\gamma}_a$ (the speed at which the circle trajectory is draw), and the time t:

$$\mathbf{R}_a(\beta_a, \dot{\gamma}_a, t) = \mathbf{R}_z(\dot{\gamma}_a t)\mathbf{R}_y(-\beta_a) \tag{4.3}$$

The product of the rotation matrices in $\mathbf{R}_z(\dot{\gamma}_a t)$ and $\mathbf{R}_y(-\beta_a)$ creates a rotation matrix $\mathbf{R}_a(\beta_a, \dot{\gamma}_a, t)$ describing the rotation about both of those axes.

The model describes the trajectory of the UHMD for an RPM rotating to exert a torque on the UHMD, while also rotating along a circular trajectory in the xy-plane with the aim of determining bounded behaviour by obtaining an indefinite but theoretically infinite circular trajectory with the UHMD (without drifting out of said circle).

The model requires the following parameters to characterise the UHMD and its environment: the density of the medium, the density of the UHMD head, the density of the UHMD tail, the magnetic moment, as well as geometric parameters for the UHMD (length, helix radius, pitch, wire diameter and head radius).

The specific input parameters that determine the behaviour of the UHMD are taken to be distance between the magnet and the microrobot, the pitch angle of the magnet, the curvature of the circle drawn by the magnet, the angular velocity at which said circle is drawn, and the actuation frequency.

4.1.1 Procedure and Results

After inputting the required characteristic parameters, a binary search method was used to attempt to find the necessary inputs for a bounded response. A range of frequencies from 1-30 Hz were investigated, with distances from 20-50 mm, while the pitch angle of the magnet was kept to a constant 4 deg, and the curvature and angular velocity of the circular trajectory varied between 20 and 45 deg and 1.8 and 0.5 deg $/s$ respectively.

However, ranges this large were investigated because determining comprehensive responses with the model was not straight-forward, and in fact, remained inconclusive. This can be seen in the Figures 5.4, which are supposed to represent the beginning of a circular trajectory (with a slow

magnet angular velocity), representing instead the movement of the UHMD at high and irrational speeds.

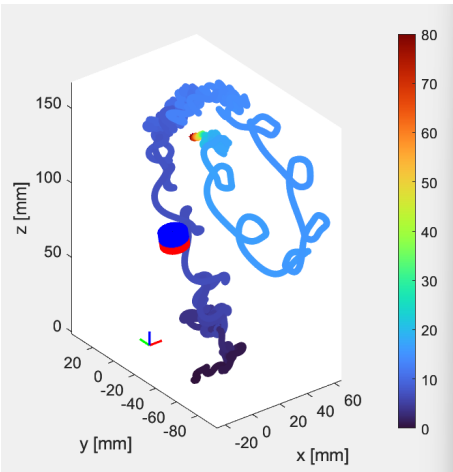

(a)

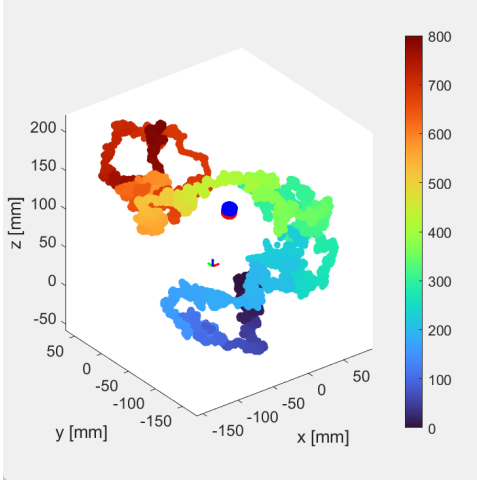

(b)

Figure 4.1: Results of the Circular RFT Based Matlab Model, showing the position of the UHMD as a function of time, (time represented by the colored bar)

Attempts at calibrating other parameters aside from the defined input parameters (such as the time step and length of the simulation) were unsuccessful, so no quantitative conclusions were derived from this Matlab model. However, during the systematic changing of the frequency input, it was noted that the simulation became slightly more cohesive at higher frequencies, in the range of 20-40Hz. This proved useful later during the experimental procedures, as a way to determine the scale of the frequency with which to work with. Due to the time consuming nature of obtaining the results and the multitude of parameters to tune, it was instead decided a different model could be attempted

4.2 COMSOL

As the Matlab model gave inconclusive results, in order to gain information about the magnetic forces at work in the system, a COMSOL Model was made. Most of the settings used in the COMSOL model were adjusted after the experimental procedures in order to focus on situations with relevant parameters.

4.2.1 Description

The COMSOL model is composed of one large cubed shape, defined as a space full of Air, in which a cylindrical magnet with the properties of the RPM was placed (same dimensions and magnetic dipole moment). The UHMD was placed 4.5 cm directly under the center of the RPM.

Physics options from the AC/DC module provided by COMSOL were applied to the model. The box of air was defined as a current-free region giving the following condition for the magnetic H-Field $\mathbf{H}$: $\nabla \times \mathbf{H}) = 0$. This defines the scalar magnetic potential V_m, as ($\mathbf{H} = -\nabla V_m$). The condition for Magnetic Flux conservation was added over all three domains, establishing the equation $-\nabla(\mu_0 \nabla V_m - \mathbf{B}_r) = 0$, where μ_0 is the permeability in a vacuum, V_m is the magnetic potential, and B_r is the remnant flux density.

Magnetic Insulation was added over all domains, and the Magnet condition was applied to the RPM, specifying the North and South borders and the magnetic moment of the RPM: $18.89 Am^2$. The materials of the UHMD and RPM were specified, Nickel (as an approximation) and NdFeB Grade-N45 respectively.

A force and torque calculation was carried out during the simulation to determine the amount of force acting on the UHMD on behalf of the RPM, which uses the integration of Maxwell's stress tensor over the outer boundary of the UHMD (requiring also a vector direction for the torque axis).

A partial validation of the model was carried out by increasing and decreasing the size of the mesh by 2.5, and determining that no change occurred in the first four significant figures of the calculated values. With the Multiphysics aspect of COMSOL, the model could be expanded to

include fluid dynamics and gravitational effects, but due to computational and time constraints, the model was not explored further.

4.2.2 Results

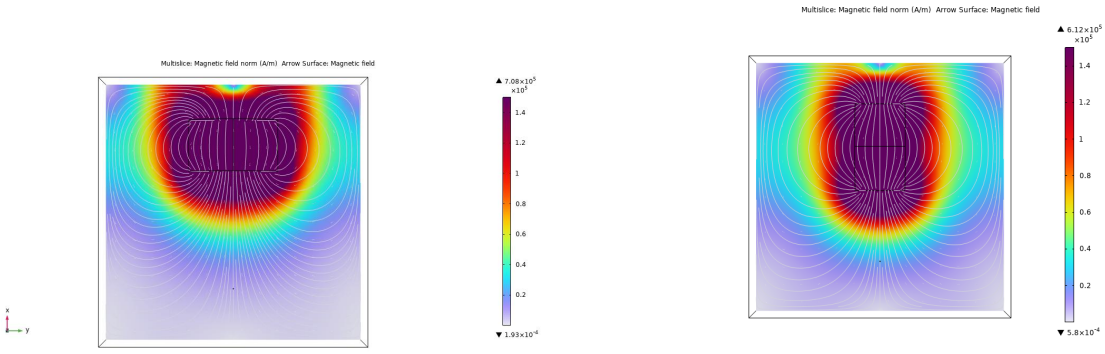

(a) (b)

Figure 4.2: Simulated Magnetic Field norm (A/m) for a magnet during rotation at (a) 0 deg and (b) 90 deg, with a microrobot in the field

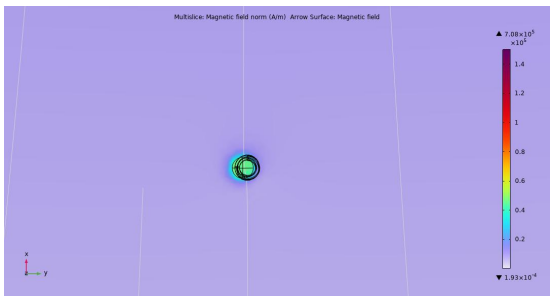

Figure 4.3: Magnified Image of Figure 4.2 (a) to focus on the Magnetic Field Near the UHMD

The results of this model include graphical plots for the Normalised Magnetic Field, used to check whether the simulation perceived any noteworthy interaction between the RPM and UHMD. This was plotted for an RPM at two different stages of rotation: 0 deg and 90 deg, as shown in Figure 4.2. A magnified look at the effect of the field on the UHMD is shown in Figure 4.3. Aside from the graphical results, the simulation was used to calculate the force and torque acting on the UHMD at different angles. As can be seen in Table 4.1, there is no noticeable difference at 2 significant figures in the forces acting on the UHMD, indicating that in this simulation, there is little variation in the effect of the RPM on the UHMD. This was unexpected, as during the rotation (from 0 deg to 90 deg) the distance to the magnet decreases, which presumably would lead to a larger attraction.

	EM Force (N)	Axial Torque (y-axis) (Nm)
0 degrees	2.7×10^{-6}	1.0×10^{-10}
90 degrees	2.7×10^{-6}	1.0×10^{-10}

Table 4.1: Results of the Force and Torque calculations during the COMSOL simulation

Chapter 5

Experimental Method

5.1 Description

In order to investigate the behaviour of the UHMDs experimentally, a setup and method were designed to observe the movement of the microrobot through a fluid (water) when actuated by a rotating permanent magnet.

To do so, the microrobots were contained in a small glass tubes filled with water, and placed in view of a camera, to be filmed while a Rotating Permanent Magnet (RPM) a distance d_m apart, rotated at a frequency of f_a at an angle β_a to the horizontal plane, with a horizontal speed of v_a.

While all of these variables are relevant to the control of the UHMD, the experiment was simplified due to physical and timeliness restrictions (further elaborated in Section 5.3.1), such that the angle of the RPM (β_a) remained constant and near-zero, and the RPM did not displace horizontally ($v_a = 0$).

5.2 Setup and Design

The UHMDs were put in a glass square cuvette filled with filtered water, which was then placed on the stage of a Keyence Digital Microscope with an added white background and a block of squared paper to mark initial distance PHM. The microscope camera was tilted at 90 degrees to film the horizontal movement of the UHMD and leave space above the cuvette for the RPM, which consisted of a large cylindrical magnet on a rotating attachment, annexed to a KUKA Robotic Arm in order to control its placement and position.

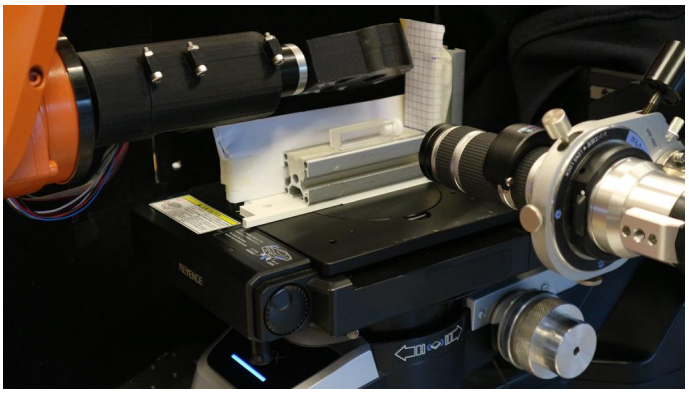

Figure 5.1: Overview of Experimental Setup

5.2.1 Cuvettes/Containment

Initially, the UHMDs were held in 10 mL cylindrical test tubes, but due to the visual distortion caused by the curvature of the glass surface, any images or videos of the microrobots were unusable. The UHMDs were instead placed in 10x10x380 mm square-shaped cuvettes (3.5 mL) with clear, straight sides, borrowed from the Chemistry SLT Labs (Student Laboratories Twente), by using 2 mL pipettes. These cuvettes were also significantly shorter than the test tubes. The cuvettes

chosen were to be 10mm wide in order to avoid edge effects influencing the swimming motion of the microrobots. The further the UHMDS are from the walls, the less interference the change in motion at the container boundaries has on their motion. A width of at least 10 times the size of the microrobot in each direction was advised, a condition which the cuvettes fulfilled.

At first, the experiments were carried out simply by applying the magnetic rotation to the UHMD swimming freely in the cuvette, as there was little way to control the starting point of the UHMD in each experiment. But in an effort to improve the consistency and reproducibility of the results, a small plastic tube (0.4 cm in diameter) was attached to the inner side of the lid of the cuvette (As seen in Figure 5.2), from which the UHMD was be located at the beginning of each experiment. This resulted in an consistent starting point for the measurements.

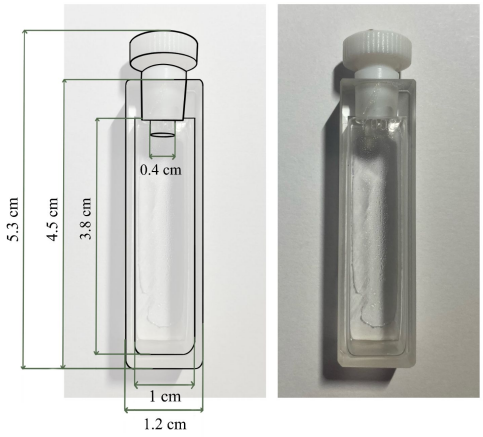

Figure 5.2: Dimensions of the cubed cuvettes used as containers.

5.2.2 Keyence Microscope

Different cameras were tried in the process of designing the setup, as the microrobot was difficult to observe with sufficient clarity, as shown in Figure 5.3. Attempts at filming the motion of a microrobot were made with a phone camera (specifically an iPhone SE) and with a digital camera available in the SRL lab, but the magnification was not enough and the microrobot remained out of focus.

A Keyence Digital Microscope of the VHX-7000 series, borrowed from the Microscopy Lab of the MS3 department at the University of Twente, had a reliable level of maneuverability and manual or automatic adjustment of focus that made it suitable for this experiment.

Primarily using the 20x and 30x magnification. The distance between the cuvette and the microscope ranged from 5 to 10 cm, varying due to the need to adjust the focus of the microscope during the movement of the robot.

(a) (b) (c)

Figure 5.3: Images taken of a micro-robot with three different cameras: (a) Cropped image from an iPhone Camera at maximum magnification, (b) Cropped image from a Blackfly S-BFS-U-13Y3C camera, (c) Image from the Keyence Microscope at 20x magnification. The Keyence provides the sharpest image of the robot.

5.2.3 Rotating Permanent Magnet

The Rotating Permanent Magnet (RPM) used was a wide, flat cylindrical magnet made of NdFeB Grade-N45, with a radius of 17.5mm and height of 20.0mm, with a dipole moment of $18.89Am^2$ encased in a black casing, attached to an industrial robotic arm (the KUKA KR 10 R1100-2). The RPM itself was powered by a motor controlled by a Matlab script, in which the rotational

frequency and time interval could be customised for different experiments. Its attachment to the robotic arm served the purpose of making the trajectory of the RPM easily controllable with a software designed for generating robot paths (RobotDK). This would have been used to automate the linear horizontal movement of the RPM, however, when testing the set-up it was made apparent that a horizontal movement of the RPM would not be necessary (as further elaborated in Section 5.2.5). This meant that the moving function of the KUKA Arm remained mostly unused except when preparing the setup, though the speed of the movements was set to the slowest settings for safety reasons anyway.

5.2.4 Additional Equipment

Other elements added to this set up include: a white background to provide contrast against the microrobot and therefore better focus; a 5cm high block to elevate the cuvette to the same height as the microscope, ensuring the same view for all measurements; and the distance marker, another block standing upright next to the cuvette with a squared paper cover, used to mark the distance between the cuvette and RPM at different measurements without displace equipment to measure said distance with a ruler.

5.2.5 Setup Overview and Limitations

Due to the fragility and importance of the Keyence Microscope, it was determined that the minimum distance between the centerline of the RPM and the cuvette (a distance labelled d_m in Figure 5.4b) was 3.5 cm. This gave extra space in case of any sudden (but consistently slow, due to the settings of the KUKA Arm) unplanned movements of the RPM.

The angle of the swimming microrobot, dictated by the angle of the RPM proved to be problematic to vary. The adhesive used to add the starting-point tube to the cuvette often caught the microrobots, especially when they began movements at angles other than parallel to the tube sides. After losing one of three available microrobots to the glue lining the tube, as it proved to be permanently attached, the experiment was simplified to have a constant β_a to the horizontal: measured to be $0\,\text{deg} \pm 4\,\text{deg}$.

As is visible in Figure 5.4a, the RPM is large in comparison to the cuvette, and especially the field of view through the Keyence microscope (Figure 5.3). Even without moving the RPM horizontally, during set-up testing, the microrobot would reach the end of the field of view of the microrobot before it left the range of the effect of the RPM. This limitation in the measurable range of motion for the microscope, as well as the extra conditions required to synchronize the rotational and linear movements of the RPM led to the experiment getting simplified further: the variable of the horizontal speed of the RPM ($v_a = 0$) was removed.

Removing the two variables v_a and β_a made the experimental process much easier, as the number of values and settings to be measured was reduced, so more of the time could be focused on repeated measurements.

The overview of the final setup is presented in Figures 5.4a and 5.1, with distances specified in Figure 5.4b.

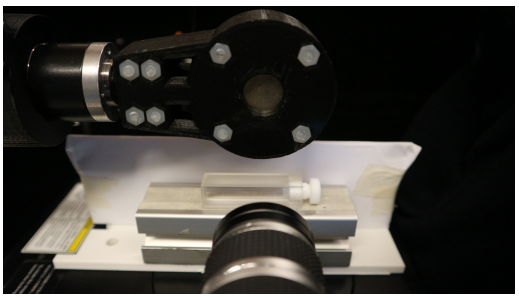

(a)

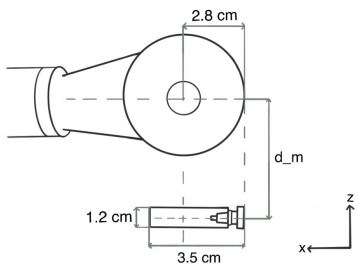

(b)

Figure 5.4: (a) ZX-Plane view of the setup, from the direction of the microscope. (b) Diagram of the ZX-plane view of the setup, labelled with distances relevant for the setup

5.3 Experimental Procedure

The experimental method consisted of exploring the frequency range $f_a = 10 - 40Hz$ and the distance range $d_m = 3.5 - 4.5cm$ with the RPM held at a constant angle of approximately 0 deg and a horizontal velocity of the RPM of $v_a = 0$. A single microrobot was used for the final measurements, due to the fact the two of them became unusable throughout the experimental procedure.

5.3.1 Noted Interferences

Although the water used in the cuvettes was filtered before use, between measurement days the dust inside the containers would accumulate and form larger dust mites. Aside from the water requiring regular replacement and the way the dust interfered in the filming, this was problematic due to the fact that the microrobots were very susceptible to getting caught in these pieces of dust, as shown in Figure 5.5 (a) and (b). Once the microrobots stuck to the dust, it would interfere with their movement and stop them from rotating as efficiently (increasing the drag of the robot). For the most part, shaking the cuvettes or using a pipette to blow air at the microrobot and dust would separate them, but one of the microrobots was put aside due to an unremovable dust mite.

(a) (b) (c)

Figure 5.5: Two images of a microrobot caught in dust in front of a (a) black background (b) white background, and an image of a microrobot stuck on the side of a tube.

The microrobots were also sensitive to surfaces, and often adhered to not only the adhesive used to add the starting-point tube (which caused another of the microrobots to be removed from the experiment), but also any of the thin sides of said tube, as shown in Figure 5.5 (c).

5.3.2 Measurement Method

The first step of each measurement was to ensure the microrobot was placed in the starting tube attached to the cuvette lid. As the microrobot could not be moved manually, this had to be done by tilting the cuvette at a variety of angles, to make the microrobot float into the tube (ensuring that it did not fall far enough into the tube to make contact with the adhesive on the cuvette lid).

Then the cuvette was placed into its position before the Keyence Microscope, under the RPM, as shown in Figure 5.4a. The recording function of the Keyence would be initiated, and then the RPM would be started (having been set to the required frequency).

Changing the frequency for an experiment was done by changing the necessary variable in the RPM Matlab script, and changing the distance between the cuvette and RPM was done by raising one of the KUKA Robotic Arm joints to an increased or decreased height, while maintaining the joint of the RPM parallel to the ground.

First, measurements were taken for frequencies from 10-40Hz, in intervals of 10Hz, for distances of 3.5cm, 4cm and 5cm. Then, after narrowing down the frequencies and distances that gave more bounded responses, measurements were taken for frequencies between 20-30Hz in intervals of 2Hz, at distances of 4cm and 4.2 cm.

5.4 Processing

The results of the Keyence recordings were AVI files, filmed at 30 frames per second. The videos that had been recording for longer than 8 minutes were then clipped, to make processing easier. All videos were then individually passed into the video tracking software *Tracker*, where the position

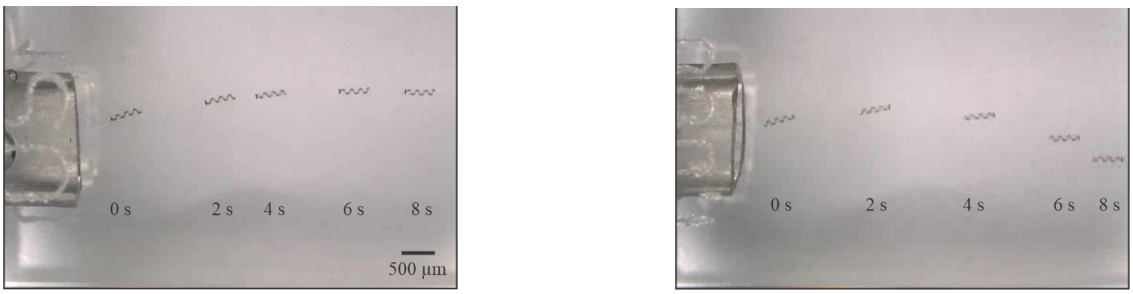

(a) (b)

Figure 5.6: Two filmed trajectories of the helical microrobot (vertically inverted). Image (a) taken at $f_a = 25Hz$, $d_m = 4.5cm$, and the robot drifts downwards due to the strong effect of gravity (falling). Image (b) taken at $f_a = 30Hz$, $d_m = 4.1cm$, where due to the closer distance to the RPM the robot drifts upwards (unbounded attraction)

of the head of the microrobot was tracked in each frame, resulting in a a dataset of distances from the robot to its initial starting point over a time period.

For each frequency and distance, two to three measurements were taken, and for each measurement, the collected dataset were averaged and simplified to represent the gain (γ) as defined in the Chapter 2.1, by defining trajectory (such as those shown in Figure 5.6) as the difference between the starting and final position of the robot (d_f, in meters) and combining it with the chosen distance between the starting point of the robot and the RPM (d_m).

$$\gamma := \frac{\min({}^{\mathrm{a}}p_{\mathrm{h}_z}(t)) - \max({}^{\mathrm{a}}p_{\mathrm{h}_z}(t))}{{}^{\mathrm{a}}p_{\mathrm{h}_z}(t_0)} = \frac{d_f}{d_m} \tag{5.1}$$

5.5 Results

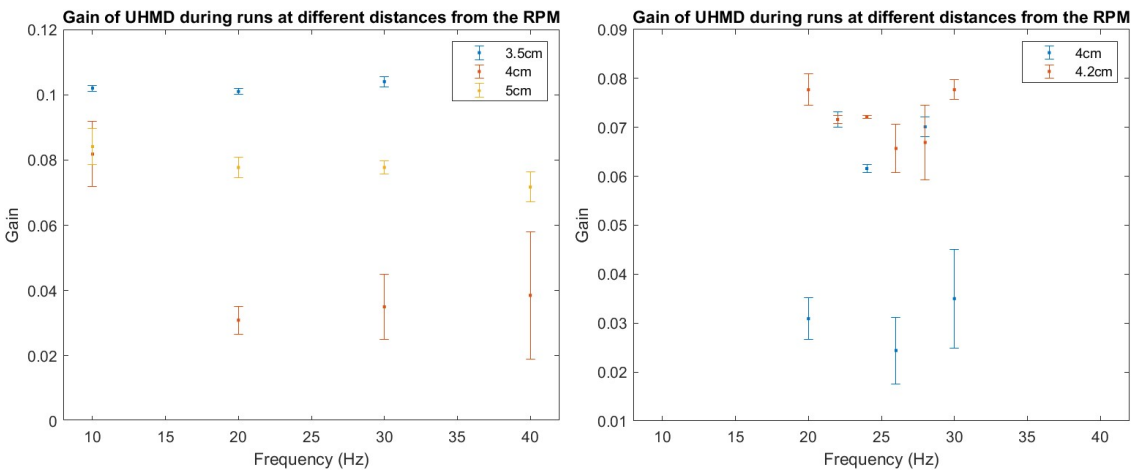

(a) (b)

Figure 5.7: Graphs representing the Gain against the frequency f_a for different distances d_m. Graph (a) is measurements from 10-40Hz in intervals of 10Hz, at distance of 3.5, 4 and 5cm. Graph (b) is measurements from 20-30Hz in intervals of 2Hz, at distances of 4 and 4.2 cm

After processing, the results of the experiments can each be classified into one of three categories: a case of unbounded attraction, where the microrobot drifts upwards into the upper wall of the cuvette (similar, but further distance than Figure 5.6 (b)), in direction of the magnet; a case of a falling microrobot, where the microrobot falls downwards onto the lower wall of the cuvette (similar, but further distance than Figure 5.6 (a)); and a case of bounded response, where the microrobot does not hit either boundary before it leaves the field of vision of the microscope.

The video results were processed from videos into a gain value corresponding to a frequency f_a and distance d_m, but in this process, both unbounded responses (falling and attraction) are presented the same way. This is due to the fact that the maximum of the absolute distance between

the initial and final points of the robot (as used for equation 5.1) is approximately the same for both cases, as the top and bottom walls are equidistant from the starting point. This creates a clear difference between the unbounded responses and the measurements in which the microrobot remained in a more or less straight line, as seen in Figures 5.7 (a) and (b), where the lower plot point on the graph indicate much straighter runs.

Figures 5.7 (a) and (b) show the average gain of the measurements taken at each of the frequencies and distances plotted. Given that a lower gain represents less change in the trajectory of the microrobot, the best results are shown in both Figure 5.7 (a) and (b), to be at frequencies between 20 and 30, at a distance of 4cm, resulting in gains around or less than 0.04, which is considerably lower than the gains of around 0.1 that most of the unbounded responses exhibit. The unbounded responses (which mostly occurred for gains between 0.07 and 0.12) do not all have the same gain, due to the fact that not all the runs had the maximal distance (that between the starting point and the wall of the cuvette) in the same direction or within the limit of the field of view, leading to small discrepancies in the value of the gain.

Some frequencies and distances led to a mixture of unbounded and straight responses, leading to points with large error bars, plotted in areas not decisively bounded or unbounded.

Chapter 6

Conclusion

6.1 Conclusion

The purpose of this research was attempt to apply established motion control of millimeter-sized UHMDs to micro-sized UHMDs and examine differences between the modelled and measured propulsion of the microrobot.

One of the limiting factors of the approach used to reach this purpose was the lack of a certain value for the magnetic moment of the UHMD. The volume-based calculation to verify or correct the EDX measurements and change the calculation of the magnetic moment was only carried out after some of the inconsistencies in the RTF model were fixed by reducing the magnetic moment parameter that had been calculated from the EDX measurement. Although, for this investigation there was not enough mass to carry out a VSM measurement, it would have brought more certainty to the magnetic parameters used in the simulations.

The aim of applying previously validated theoretical models to predict bounded responses for the microrobots was unsuccessful, as the Matlab model did not provided any interpretable results, bounded or unbounded. The COMSOL model was carried out as an investigation into the Magnetic behaviour associated with the determined parameters, but was not extended to include fluid dynamics, or utilised further.

Bounded behaviour was determined in the experimental investigation of this thesis, with enough bounded responses to be able to identify patterns and determine the parameters for the bounded response with the least drift within the frequency and distance ranges measured. It was determined that the previously established guideline [2] that bounded behaviour occurs for gains $0 < \gamma < 1$ for the given equation of gain holds best when the UHMD is not as limited in its range of vertical motion as it was for this experiment. Most bounded behaviour measured was exhibited in gains of 0.06 or below, and unbounded behaviour ranged from 0.06 to 0.12.

In conclusion, during this investigation, bounded responses were obtained experimentally with the helical microrobots, but further investigation is necessary into whether the previously designed model can predict bounded behaviour accurately, as the results from the simulations were inconclusive.

6.2 Further Work

In order to fully answer the proposed research question, further work would have to be done, such as correctly calibrating the integration parameters of the RTF Matlab Code, and/or expanding the COMSOL model to include fluid dynamics and gravitational forces, providing an image of the force-balance. Experimentally, further work should be done to investigate the effect of the angle of attack of the UHMD. Furthermore, exploring different microscopy/camera equipment with a wider field of view, could make it possible to further investigate the UHMD trajectories when the RPM is translated horizontally.

Bibliography

[1] Arthur W. Mahoney. Advanced methods for controlling untethered magnetic devices using rotating magnetic fields. 2014.

[2] Leendert-Jan W. Ligtenberg and Islam S.M. Khalil. Input-output boundedness of a magnetically-actuated helical device. In *2023 IEEE International Conference on Robotics and Automation (ICRA 2023)*, pages 5433–5438, United States, May 2023. IEEE. 2023 IEEE International Conference on Robotics and Automation (ICRA 2023) ; Conference date: 31-05-2023 Through 02-06-2023.

[3] Hooper W. C. Critchley S. E. Ortel T. L. Beckman, M. G. Venous thromboembolism: a public health concern. *American journal of preventive medicine*, 2010.

[4] Ahmed El Sharkawy Ramez R. Moustafa Ahmet Fatih Tabak Mohamed E. Mitwally Sarah Hesham Nabila Hamdi Anke Klingner Islam S. M. Khalil, Dalia Mahdy and Metin Sitti. Mechanical rubbing of blood clots using helical robots under ultrasound guidance. *IEEE Robotics and Automation Letters (RAL) 2018 IEEE International Conference on Robotics and Automation (ICRA)*, 2018.

[5] Abdelrahman Hosney, Joseph Abdalla, Ibrahim S. Amin, Nabila Hamdi, and Islam S.M. Khalil. In vitro validation of clearing clogged vessels using microrobots. In *2016 6th IEEE International Conference on Biomedical Robotics and Biomechatronics, BioRob 2016*, 2016 6th IEEE International Conference on Biomedical Robotics and Biomechatronics (BioRob), pages 272–277, United States, July 2016. IEEE. Publisher Copyright: © 2016 IEEE.; 6th IEEE RAS/EMBS International Conference on Biomedical Robotics and Biomechatronics, BioRob 2016, BioRob 2016 ; Conference date: 26-06-2016 Through 29-06-2016.

[6] Sarthak Misra Islam S.M. Khalil, Anke Klingner. *Mathematical Modeling of Swimming Soft Microrobots*, volume 1. Elsevier Inc, 2021.

[7] Anwar Ul-Hamid. *A beginners' guide to scanning electron microscopy*, volume 1. Springer, 2018.

[8] Purdue university, scanning electron microscope. https://www.purdue.edu/ehps/rem/laboratory/equipment Accessed: 2023-07-09.

[9] Hollis Williams. Sem for conductive and non-conductive specimens. *Physics Education*, 56(5):055034, aug 2021.

[10] The difference between sem and optical microscopes. https://www.thermofisher.com/nl/en/home/materials-science/learning-center/applications/sem-optical-microscopes-difference.html: :text=In Accessed: 2023-07-12.

[11] A.O. Adeyeye and G. Shimon. Chapter 1 - growth and characterization of magnetic thin film and nanostructures. In Robert E. Camley, Zbigniew Celinski, and Robert L. Stamps, editors, *Magnetism of Surfaces, Interfaces, and Nanoscale Materials*, volume 5 of *Handbook of Surface Science*, pages 1–41. North-Holland, 2015.

[12] Sina Ebnesajjad. Chapter 4 - surface and material characterization techniques. In Sina Ebnesajjad, editor, *Surface Treatment of Materials for Adhesive Bonding (Second Edition)*, pages 39–75. William Andrew Publishing, Oxford, second edition edition, 2014.

[13] Q. Wei, F. Huang, and Y. Cai. 2 - textile surface characterization methods. In Q. Wei, editor, *Surface Modification of Textiles*, Woodhead Publishing Series in Textiles, pages 26–57. Woodhead Publishing, 2009.

[14] About nickel and its applications. https://nickelinstitute.org/en/about-nickel-and-its-applications/properties-of-nickel/. Accessed: 2023-06-22.

[15] Density of gold. https://www.xetra-gold.com/en/gold-news/news/figure-of-the-month-19320-gcm3/: :text=In Accessed: 2023-06-22.

[16] Material safety data sheet, ip-dip. https://www.uni-muenster.de/imperia/md/content/mnf/ip-dip$_p hotoresist.pdf. Accessed : 2023 - 06 - 22$.

[17] Magnetic dipole - encyclopedia britannica. https://www.britannica.com/science/magnetic-dipole. Published: 2022-08-04.

[18] David Halliday. *Fundamentals of Physics - 10th Edition*, volume 1. Wiley, 2004.

[19] George D. Greenwade. The Comprehensive Tex Archive Network (CTAN). *TUGBoat*, 14(3):342–351, 1993.

[20] Cichomski M. Zieliński M. Klepka T. Sroczyński D. Fenyk A. Miekoś, E. Modification of the properties of polymer composites in a constant magnetic field environment. *Materials (Basel, Switzerland)*, 14(14):3806, 2021.

[21] J. C. Slater. The ferromagnetism of nickel. ii. temperature effects. *Phys. Rev.*, 49:931–937, Jun 1936.

[22] W. G. Henry and J. L. Rogers. Xxi. the magnetic susceptibilities of copper, silver and gold and errors in the gouy method. *The Philosophical Magazine: A Journal of Theoretical Experimental and Applied Physics*, 1(3):223–236, 1956.

[23] C.M. Hurd. The magnetic susceptibility of silver and gold in the range 6–300°k. *Journal of Physics and Chemistry of Solids*, 27(9):1371–1374, 1966.

[24] Annika Venäläinen, Pasi Jalkanen, Vladimir Tuboltsev, Kristoffer Meinander, Alexander Savin, and Jyrki Räisänen. Ferromagnetism in bare gold nanoagglomerates produced by nanocluster deposition. *Journal of Magnetism and Magnetic Materials*, 454:57–60, 2018.

[25] Vladimir Tuboltsev, Alexander Savin, Alexandre Pirojenko, and Jyrki Räisänen. Magnetism in nanocrystalline gold. *ACS Nano*, 7(8):6691–6699, 2013. PMID: 23829643.

[26] Pierce W. Selwood. Applications of magnetochemistry to polymers and polymerizationl. 2006.

[27] Crangle J. and Goodman G. M. The magnetization of pure iron and nickel. *R. Soc. Lond*, 1971.